

In situ Irradiated XPS Investigation on S-Scheme $\text{TiO}_2@Zn\text{In}_2\text{S}_4$ Photocatalyst for Efficient Photocatalytic CO_2 Reduction

Libo Wang, Bei Cheng, Liuyang Zhang,* and Jiaguo Yu*

Reasonable design of efficient hierarchical photocatalysts has gained significant attention. Herein, a step-scheme (S-scheme) core-shell $\text{TiO}_2@Zn\text{In}_2\text{S}_4$ heterojunction is designed for photocatalytic CO_2 reduction. The optimized sample exhibits much higher CO_2 photoreduction conversion rates (the sum yield of CO , CH_3OH , and CH_4) than the blank control, i.e., $Zn\text{In}_2\text{S}_4$ and TiO_2 . The improved photocatalytic performance can be attributed to the inhibited recombination of photogenerated charge carriers induced by S-scheme heterojunction. The improvement is also attributed to the large specific surface areas and abundant active sites. Meanwhile, S-scheme photogenerated charge transfer mechanism is testified by in situ irradiated X-ray photoelectron spectroscopy, work function calculation, and electron paramagnetic resonance measurements. This work provides an effective strategy for designing highly efficient heterojunction photocatalysts for conversion of solar fuels.

Recently, a novel step-scheme (S-scheme) heterojunction was proposed and has attracted researchers' attention.^[23–36] Usually, S-scheme heterojunction consists of reduction photocatalyst (RP) and oxidation photocatalyst (OP). Besides, the directional migration of free electrons will lead to band bending and internal electric field (IEF) at their interface owing to the work function difference. Notably, under the influence of IEF, the photogenerated electrons of OP with weak reduction ability can recombine with the photogenerated holes of RP with weak oxidation ability; while those with strong redox abilities are preserved. Therefore, reasonable construction of TiO_2 -based S-scheme heterojunction is of great significance to improve photocatalytic reaction performance.

1. Introduction

Photocatalytic CO_2 reduction (PCR) into chemical fuels under mild conditions is recognized to be promising for alleviating energy crisis and greenhouse effect.^[1–11] Therefore, reasonable design of efficient photocatalysts is necessary to improve PCR performance. Among various semiconductor photocatalysts, TiO_2 has received great attention due to its non-toxicity, cost-effectiveness, and excellent chemical stability.^[12–16] However, as a typical oxidation photocatalyst, unitary TiO_2 suffers from low activity owing to its poor photoreduction ability and fast recombination of photogenerated electrons and holes.^[12–15] To overcome these drawbacks, various solutions have been employed.^[17–20] Among them, heterojunction construction is proved to be an effective strategy due to the efficient transfer and separation of photogenerated charge carriers.^[21–23]

Apart from the charge carrier separation, the morphology of photocatalysts is another important factor to influence the photocatalytic performance.^[15,17,19,37,38] Photocatalysts with hollow structures have attracted great attention owing to manifold advantages including larger specific surface area, abundant active sites, shortened diffusion distance as well as improved light reflection and scattering.^[37,39–44] Therefore, the design of hollow S-scheme heterojunction photocatalyst is of vital importance to enhance photocatalytic performance.

$Zn\text{In}_2\text{S}_4$, as a typical reduction photocatalyst, stands out for its layered structure, narrow bandgap, suitable redox potentials, and good chemical stability. And it has been used for various photocatalytic applications including hydrogen production, CO_2 reduction, and organic degradation.^[45–51] Unfortunately, pristine $Zn\text{In}_2\text{S}_4$ photocatalyst shows low photocatalytic efficiency owing to the fast recombination of photogenerated charge carriers.^[45–49] Considering the suitable match of band gap of $Zn\text{In}_2\text{S}_4$ and TiO_2 for S-scheme heterojunction,^[27,52] we construct the hollow $\text{TiO}_2@Zn\text{In}_2\text{S}_4$ core-shell structure. Up to now, to the best of our knowledge, it has never been reported.

Herein, we grow $Zn\text{In}_2\text{S}_4$ nanosheets on the outer surface of TiO_2 hollow spheres by in situ chemical bath deposition reaction. This rational design is not only able to provide large specific surface areas and abundant reaction sites for PCR reaction, but also can effectively suppress the recombination of useful photogenerated electrons and holes. As a result, the optimized $\text{TiO}_2@Zn\text{In}_2\text{S}_4$ heterojunction exhibits high PCR performance, and the total CO_2 photoreduction conversion rates (the sum yield of CO , CH_3OH and CH_4) are obviously higher than those of blank $Zn\text{In}_2\text{S}_4$, TiO_2 , and ex situ prepared TiO_2 - $Zn\text{In}_2\text{S}_4$ composite. Finally, S-scheme mechanism is also thoroughly analyzed and discussed in this work.

L. Wang, B. Cheng, L. Zhang, J. Yu
State Key Laboratory of Advanced Technology for Materials Synthesis and Processing
Wuhan University of Technology
Wuhan 430070, P. R. China
E-mail: zly2017@whut.edu.cn; yujiaguo93@whut.edu.cn
J. Yu
Laboratory of Solar Fuel
Faculty of Materials Science and Chemistry
China University of Geosciences
388 Lumo Road, Wuhan 430074, P. R. China

 The ORCID identification number(s) for the author(s) of this article can be found under <https://doi.org/10.1002/sml.202103447>.

DOI: 10.1002/sml.202103447

2. Results and Discussion

The preparation processes of hierarchical $\text{TiO}_2@Zn\text{In}_2\text{S}_4$ core-shell hollow spheres (CSHS) are illustrated in **Figure 1a**. Firstly, SiO_2 spheres with average diameters of 350 nm as the hard-templates are prepared by a modified Stöber method (Figure S1a, Supporting Information).^[53] Afterwards, TiO_2 nanoparticles are coated on the surface of SiO_2 spheres to form $\text{TiO}_2@SiO_2$ solid spheres with average diameters of 500 nm via versatile kinetics-controlled coating and thermal annealing (Figure S1b, Supporting Information).^[54] Subsequently, these $\text{TiO}_2@SiO_2$

solid spheres are etched with HF solution to remove the SiO_2 templates, and then TiO_2 hollow spheres are obtained. Field-emission scanning electron microscopy (FESEM) images clearly show that the sphere structures are intact after HF solution treatment (Figure 1b, Figure S1c, Supporting Information). Afterwards, hierarchical $\text{TiO}_2@Zn\text{In}_2\text{S}_4$ CSHS are successfully acquired by in situ chemical bath deposition. During the reaction processes, due to the positively charged surface of TiO_2 (pH = 2.5) (Figure S2, Supporting Information), the negative-charged S^{2-} ions released from the decomposition of thioacetamide can be adsorbed on the outer surface

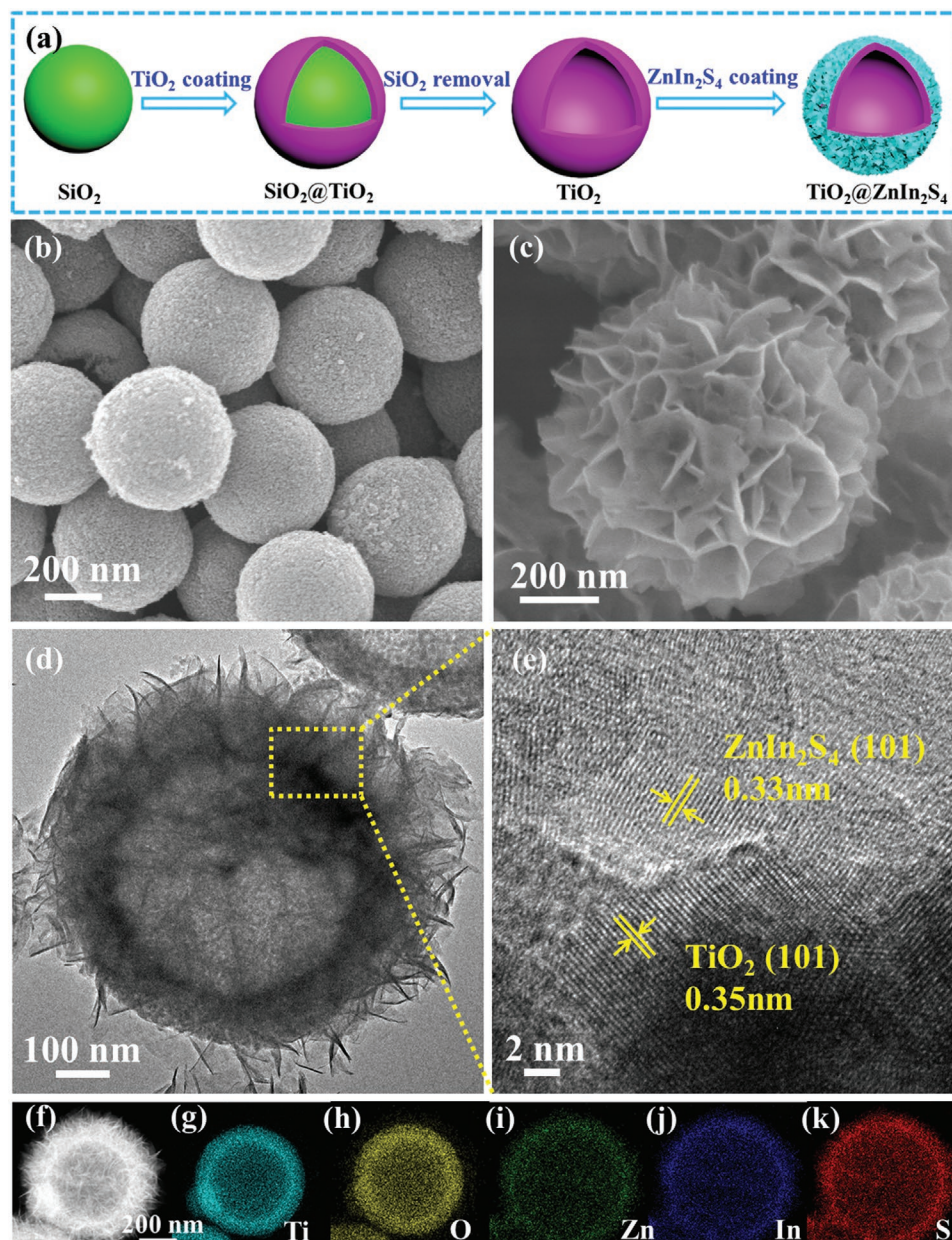


Figure 1. a) Illustration of the preparation processes of $\text{TiO}_2@Zn\text{In}_2\text{S}_4$ core-shell hollow spheres (CSHS). Field-emission scanning electron microscopy (FESEM) images of b) TiO_2 hollow spheres and c) $\text{TiO}_2@Zn\text{In}_2\text{S}_4$ CSHS. d) Transmission electron microscopy (TEM) and its corresponding e) high-resolution TEM (HRTEM) image of $\text{TiO}_2@Zn\text{In}_2\text{S}_4$ CSHS. f) High-angle annular dark-field (HAADF) image of $\text{TiO}_2@Zn\text{In}_2\text{S}_4$ CSHS. g–k) EDS mapping images of Ti, O, Zn, In, and S elements.

of TiO₂ hollow spheres through electrostatic interactions. Further reactions between positive metal ions (Zn²⁺ and In³⁺) and negative S²⁻ ions attached on TiO₂ promote the formation of the ZnIn₂S₄ nanosheets on the outer surface of TiO₂ hollow spheres with tight contact (Figure 1c). Transmission electron microscopy (TEM) image clearly validates the formation of hierarchical TiO₂@ZnIn₂S₄ CSHS (Figure 1d). Meanwhile, its corresponding high-resolution TEM (HRTEM) image indicates that the spacing of distinct lattice fringes with are 0.33 and 0.35 nm, which can be respectively indexed into the (101) planes of ZnIn₂S₄ and TiO₂ (Figure 1e). Furthermore, high-angle annular dark-field (HAADF) image (Figure 1f) and corresponding elemental mapping images (Figure 1g–k) clearly demonstrate the distribution of Ti, O, Zn, In, and S elements in TiO₂@ZnIn₂S₄ composite. Most notably, the innermost region of TiO₂ hollow sphere core and the outer ZnIn₂S₄ nanosheet shell can be distinguished. These results directly indicate that hierarchical TiO₂@ZnIn₂S₄ CSHS are successfully constructed. By contrast, in the absence of TiO₂ hollow sphere core, random aggregation of blank ZnIn₂S₄ is observed (Figure S1d, Supporting Information).

The X-ray powder diffraction (XRD) patterns were measured to identify the phase structures of samples. As presented in Figure 2a, the peaks of TiO₂ and ZnIn₂S₄ correspond to the typical diffraction peaks of anatase TiO₂ (JCPDS No. 84–1286) and hexagonal ZnIn₂S₄ (JCPDS No. 72–0773),^[45,47] respectively. Furthermore, the presence of TiO₂ and ZnIn₂S₄ in the TiO₂@ZnIn₂S₄ can be observed. Besides, compared with the pristine TiO₂ and ZnIn₂S₄, the positions of diffraction peaks in TiO₂@ZnIn₂S₄ composite are almost unchanged, indicating that the growth of ZnIn₂S₄ does not alter their respective crystal structures.

To identify the surface element composition and electronic chemical states of TiO₂, ZnIn₂S₄, and TiO₂@ZnIn₂S₄, X-ray photoelectron spectroscopy (XPS) was employed. As presented in Figure S3 (Supporting Information), XPS survey spectra indicate that Ti, O, Zn, In, and S elements can be detected in the TiO₂@ZnIn₂S₄ composite, which are in according with the EDS results. Besides, as for Ti, the peaks centered at 458.5 and 464.2 eV can be assigned to the 2p_{3/2} and 2p_{1/2} of Ti, respectively (Figure 2b).^[24,55] The peaks centered at 529.4 and 531.4 eV can be ascribed to the Ti-O bond and surface hydroxyl (–OH) group, respectively (Figure 2c).^[23,55] While for Zn, the peaks located at 1022.0 and 1045.1 eV are attributed to its 2p_{3/2} and 2p_{1/2} orbitals, respectively (Figure 2d).^[45–47] The binding energy difference is about 23.1 eV, which is typical of Zn²⁺ in ZnIn₂S₄.^[45–47] In Figure 2e, the peaks located at 444.9 and 452.5 eV can be attributed to the 3d_{5/2} and 3d_{3/2} of In, respectively, suggesting that its valence state is +3.^[45–47] In Figure 2f, the peaks centered at 161.6 and 162.8 eV, assigning to the 2p_{3/2} and 2p_{1/2} of S, respectively, is the characteristic of S²⁻ and in agreement with the literature.^[45–47] Notably, the electron binding energy of element originates from the strong Coulomb attraction between the outer electrons of atom and atomic nucleus.^[20,56,57] Meanwhile, the changes of element binding energy can directly reflect the changes of electron density.^[20,56,57] This means that the decrease of electron density can lead to the increase of binding energy. Contrarily, the decrease of binding energy is owing to the fact that the atom obtains electrons.^[20,56,57] Therefore, the binding energy change can be used to examine the direction of charge carrier transfer in heterojunction photocatalysts.^[23,27,55,58] As shown in Figure 2b,c, compared with TiO₂, the binding energies of O 1s and Ti 2p in TiO₂@ZnIn₂S₄ composite obviously

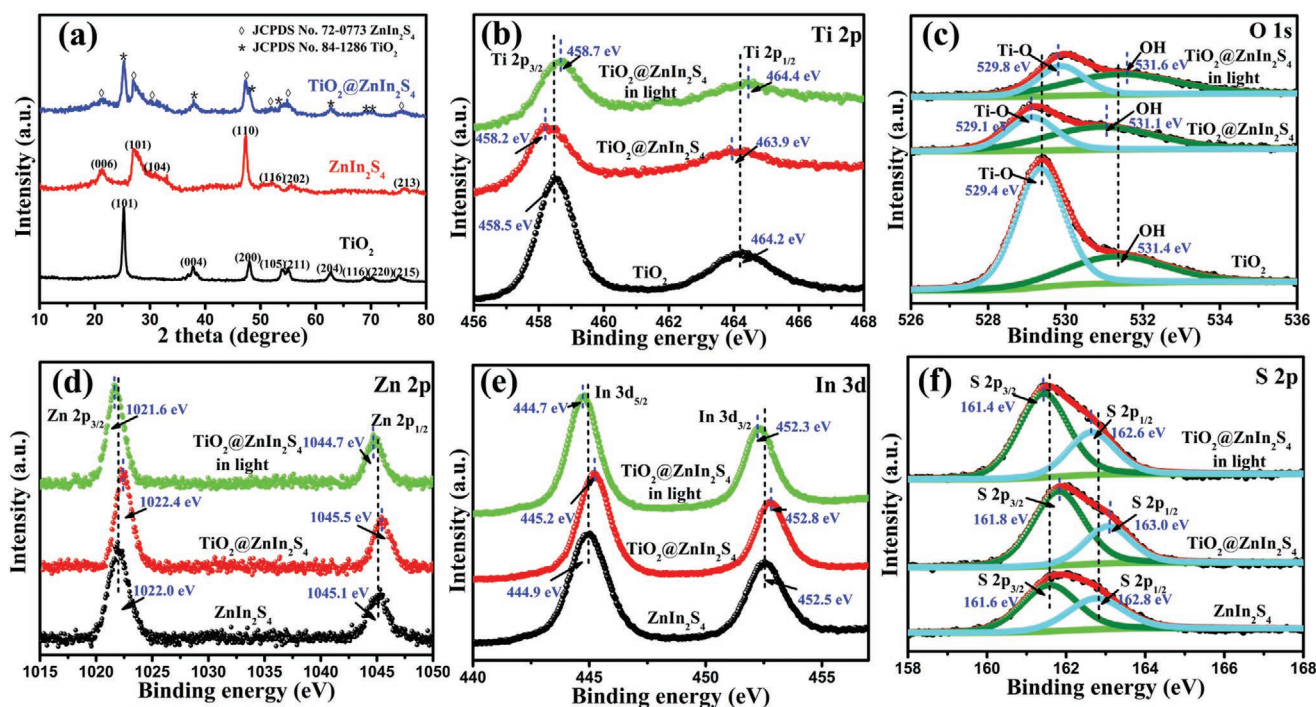


Figure 2. a) X-ray powder diffraction (XRD) patterns of TiO₂, ZnIn₂S₄, and TiO₂@ZnIn₂S₄. High-resolution X-ray photoelectron spectroscopy (XPS) spectra of b) Ti 2p and c) O 1s of TiO₂ and TiO₂@ZnIn₂S₄. High-resolution XPS spectra of d) Zn 2p, e) In 3d, and f) S 2p of ZnIn₂S₄ and TiO₂@ZnIn₂S₄.

shift toward lower energy levels in darkness, indicating an increase in the electron density of TiO_2 .^[23,55] In contrast, compared with ZnIn_2S_4 , the binding energies of Zn 2p, In 3d, and S 2p in $\text{TiO}_2@ZnIn_2S_4$ significantly shift to higher energy levels in darkness (Figure 2d–f), implying that the electrons migrate from ZnIn_2S_4 to TiO_2 . Furthermore, when in situ irradiated XPS measurements are performed,^[20,23,27,55–58] compared with $\text{TiO}_2@ZnIn_2S_4$ in darkness, the binding energies of O 1s and Ti 2p in the $\text{TiO}_2@ZnIn_2S_4$ composite under light irradiation markedly move to higher energy levels (Figure 2b,c); while the binding energies of Zn 2p, In 3d and S 2p in the nanocomposite obviously shift to lower energy levels (Figure 2d–f), suggesting the photogenerated electrons transfer from TiO_2 to ZnIn_2S_4 under light irradiation.^[27,58] Therefore, these XPS results provide important evidences of the charge carrier transfer pathway across the $\text{TiO}_2@ZnIn_2S_4$ heterojunction interface under light irradiation. In detail, the migration of photogenerated electrons from TiO_2 to ZnIn_2S_4 , matching well with the S-scheme mechanism.

Most importantly, the difference in work functions (W) or Fermi levels (E_f) for semiconductor photocatalysts is the internal driving force of charge transfer in heterojunction nanocomposite. W of TiO_2 , ZnIn_2S_4 , and $\text{TiO}_2@ZnIn_2S_4$ were obtained by Kelvin probe measurements.^[58,59] As a result, W of TiO_2 , ZnIn_2S_4 , and $\text{TiO}_2@ZnIn_2S_4$ are determined to be 4.69, 3.92 and 4.31 eV, respectively (Figure 3a, Figure S4 and Table S1, Supporting Information). E_f of samples is calculated on the basis of the following equation (1):

$$E_f = V_{ac} - W \quad (1)$$

where V_{ac} is the vacuum level (assumed as 0 eV).^[60] Thus, E_f of TiO_2 , ZnIn_2S_4 and $\text{TiO}_2@ZnIn_2S_4$ are determined to be -4.69 , -3.92 and -4.31 eV, respectively. Obviously, TiO_2 has a larger W (4.61 eV) and lower E_f (-4.61 eV), ZnIn_2S_4 has a smaller W (3.92 eV) and higher E_f (-3.92 eV) (Figure 3a). Moreover, when $\text{TiO}_2@ZnIn_2S_4$ heterojunction is formed, the electrons will transfer from ZnIn_2S_4 to TiO_2 easily until the E_f at the interface tends to equilibrate (Figure 3b). Concurrently, ZnIn_2S_4 shows upward interface band bending and is positively charged at the interface due to loss of electrons; while TiO_2 exhibits downward interface band bending and is negatively charged at the interface due to accumulation of electrons (Figure 3b). In consequence, the electrons transfer creates an IEF at the interfaces

pointing from ZnIn_2S_4 to TiO_2 (Figure 3b).^[23,24,27,55,61] When $\text{TiO}_2@ZnIn_2S_4$ heterojunction is exposed to light, electrons are excited from VB to CB of ZnIn_2S_4 and TiO_2 , respectively. Under the combined effect of IEF, interface band bending and Coulomb interaction, the photogenerated electrons in CB of TiO_2 easily transfer to VB of ZnIn_2S_4 and recombine with the photogenerated holes of ZnIn_2S_4 (Figure 3c).^[23,24,27,55,61] This interfacial charge transfer behavior of $\text{TiO}_2@ZnIn_2S_4$ heterojunction accords with the XPS results and is in agreement with the S-scheme mechanism. Meanwhile, the photogenerated holes on VB of TiO_2 and the photogenerated electrons on CB of ZnIn_2S_4 are maintained, which participate in the photocatalytic redox reaction, respectively (Figure 3c). Besides, due to the intimate interface contact between ZnIn_2S_4 and TiO_2 , the intensity of IEF at interface is greatly enhanced, which is favorable for the interfacial photogenerated charge transfer as well as effectively improve the PCR performance.

Meanwhile, the band structures of samples were measured by Mott–Schottky (M–S) and UV-vis diffuse reflectance spectra (UV-vis DRS spectra) measurements. M–S plots of TiO_2 and ZnIn_2S_4 exhibit positive slopes, suggesting that both samples are n-type semiconductors (Figure 4a).^[55,58,62,63] Moreover, the flat-band potentials (E_{fb}) of TiO_2 and ZnIn_2S_4 are -0.22 and -0.86 V (versus normal hydrogen electrode (NHE), at pH = 0. Note: The potentials in this paper are relative to that of NHE unless otherwise mentioned.), respectively. Usually, the E_{fb} of n-type semiconductor roughly equals to the conduction band (CB) potential.^[55,58,62,64] Besides, the band gap (E_g) of TiO_2 (3.20 eV) and ZnIn_2S_4 (2.43 eV) are obtained by UV-vis DRS spectra and Tauc plots (Figure 4b,c), respectively. Therefore, considering the CB positions and E_g of TiO_2 and ZnIn_2S_4 , the valence band (VB) potentials of TiO_2 and ZnIn_2S_4 are 2.98 and 1.57 V, respectively. Meanwhile, according to the above results and analysis, the band structures of TiO_2 and ZnIn_2S_4 are presented in Figure 4d. Noticeably, the reduction potentials of CO , CH_3OH and CH_4 are -0.12 , 0.03 and 0.17 V, respectively,^[27,58,65] implying that TiO_2 and ZnIn_2S_4 are thermodynamically feasible for converting CO_2 into CO , CH_3OH and CH_4 (Figure 4d).

Additionally, to further validate the S-scheme mechanism of $\text{TiO}_2@ZnIn_2S_4$ heterojunction, the electron paramagnetic resonance (EPR) spectra of hydroxyl ($\cdot\text{OH}$) and superoxide ($\cdot\text{O}_2^-$) radicals via 5, 5-dimethyl-1-pyrroline N-oxide (DMPO) were measured.^[24,27,32] The redox potentials of $\text{H}_2\text{O}/\cdot\text{OH}$ (2.37 V) or $\text{OH}^-/\cdot\text{OH}$ (2.69 V) and $\text{O}_2/\cdot\text{O}_2^-$ couples (-0.33 V) are shown

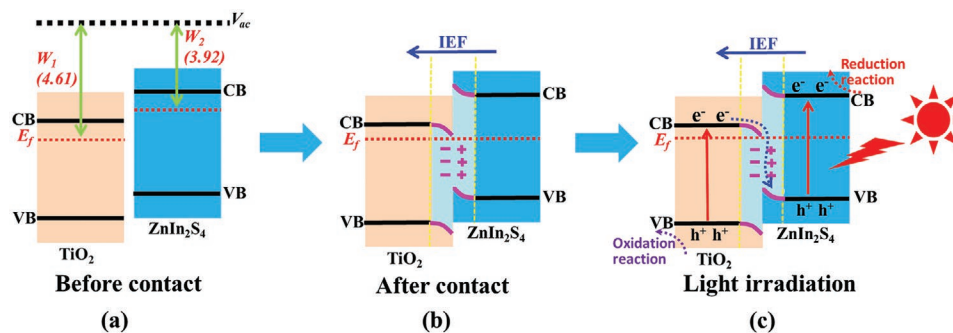


Figure 3. Schematic illustration of the S-scheme transfer mechanism between TiO_2 and ZnIn_2S_4 . V_{ac} : Vacuum level; W : Work function; E_f : Fermi level; CB: conduction band; VB: valence band; IEF: internal electric field. a) Before contact, b) after contact, and c) after contact in light.

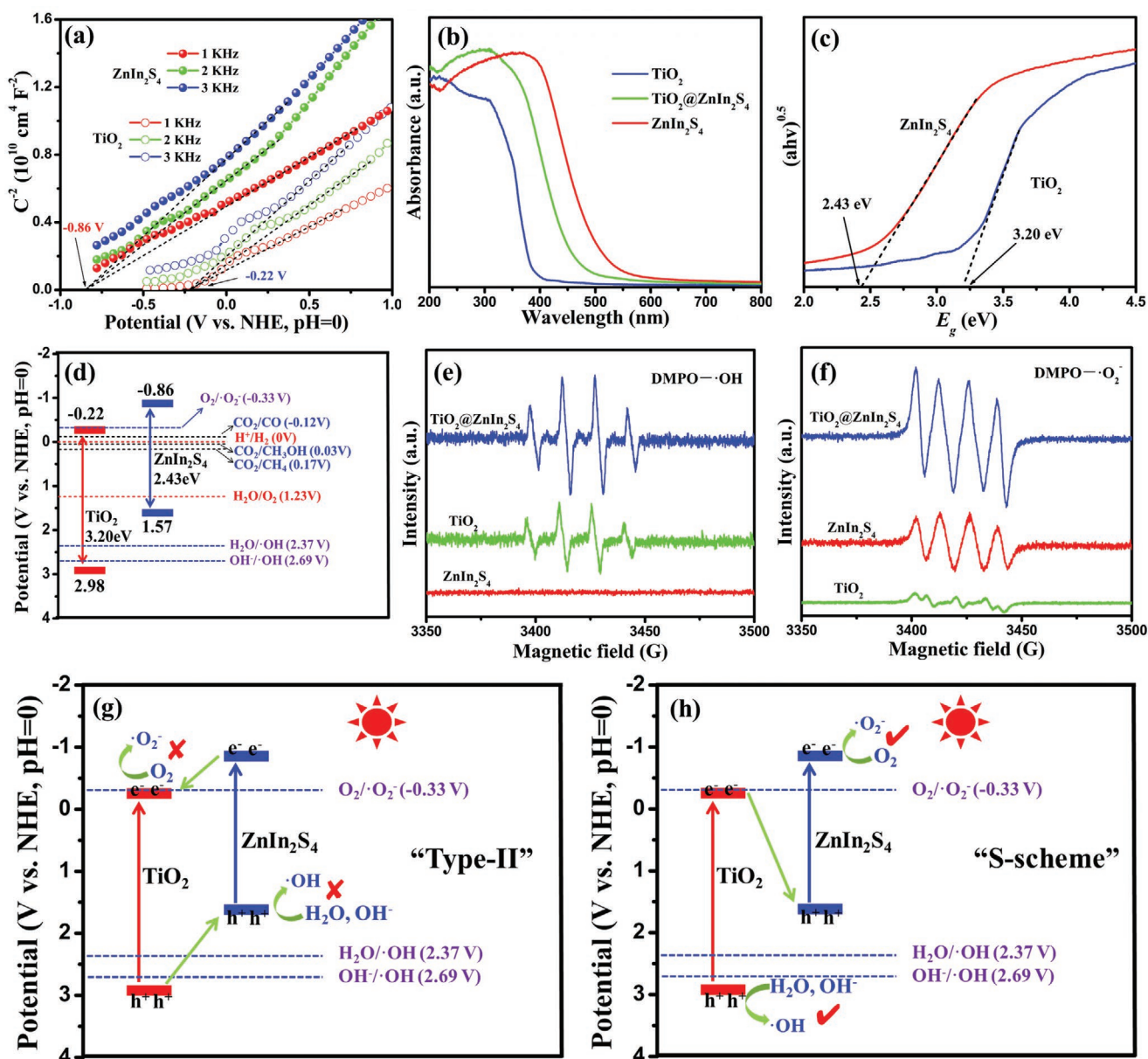


Figure 4. a) M–S plots, b) UV-vis diffuse reflectance spectra (UV-vis DRS), c) Tauc plots, and d) band structures of samples. Electron paramagnetic resonance (EPR) spectra of e) DMPO·OH adducts (in aqueous solution) and f) DMPO·O₂^{·-} adducts (in methanol solution) over TiO₂, ZnIn₂S₄, and TiO₂@ZnIn₂S₄ under illumination for 2 min. Schematic diagrams of g) conventional type-II and h) S-scheme heterojunction.

in Figure 4d.^[24,27,32] Meanwhile, EPR spectra of DMPO·OH and DMPO·O₂^{·-} adducts of TiO₂, ZnIn₂S₄ and TiO₂@ZnIn₂S₄ are detected under irradiation, respectively (Figure 4e,f). It can be seen that the DMPO·OH signal of TiO₂@ZnIn₂S₄ is obviously stronger than that of pristine TiO₂; while the DMPO·OH signal of pristine ZnIn₂S₄ is hardly observed (Figure 4e). Moreover, the DMPO·O₂^{·-} intensity of TiO₂@ZnIn₂S₄ is evidently higher than that of pristine ZnIn₂S₄; while the DMPO·O₂^{·-} intensity of pristine TiO₂ is very weak (Figure 4f). The main reason is that the oxidation potential of photogenerated holes on VB of TiO₂ (2.98 V) is more positive than the redox potential of H₂O/·OH (2.37 V) or OH⁻/·OH (2.69 V) couples; while the reduction potential of photogenerated electrons on

CB of TiO₂ (-0.22 V) is positive than the redox potential of O₂/·O₂^{·-} couples (-0.33 V) (Figure 4d).^[24,27,32] But for ZnIn₂S₄, the trend is reversed (Figure 4d). Notably, if the charge transfer mechanism of TiO₂@ZnIn₂S₄ heterojunction conforms to traditional type-II heterojunction, the generation of ·OH and ·O₂^{·-} radicals are not facilitated (Figure 4g). However, it is notable that for the DMPO·OH or DMPO·O₂^{·-} adducts, the signal intensity of TiO₂@ZnIn₂S₄ are obviously stronger than those of pristine TiO₂ and ZnIn₂S₄ (Figure 4e,f). These results indicate that the photogenerated charge transfer mechanism of TiO₂@ZnIn₂S₄ heterojunction is in agreement with the S-scheme mechanism rather than traditional type-II heterojunction (Figure 4h).^[24,27,32]

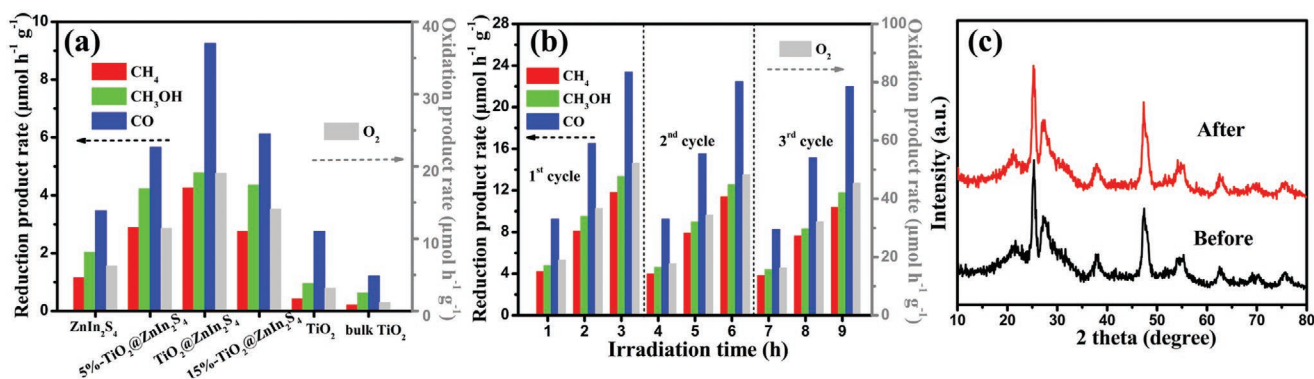


Figure 5. a) Yield of products in photocatalytic CO₂ reduction (PCR) reaction of different samples. b) Stability tests of TiO₂@ZnIn₂S₄. c) X-ray powder diffraction (XRD) patterns before and after the stability tests of TiO₂@ZnIn₂S₄.

PCR reaction activities of different samples were measured under full-spectrum irradiation. As shown in Figure 5a, CO, CH₃OH and CH₄ are the major photoreduction products of samples. Obviously, total CO₂ photoreduction conversion rates (the sum yield of CO, CH₃OH and CH₄) of TiO₂ hollow spheres (4.13 μmol h⁻¹ g⁻¹) are higher than those of bulk TiO₂ non-hollow structure sample (Figure S5, Supporting Information) (2.04 μmol h⁻¹ g⁻¹), showing the advantage of hollow structure in the PCR reaction. Besides, total CO₂ photoreduction conversion rates of 6.65 μmol h⁻¹ g⁻¹ are achieved by pristine ZnIn₂S₄ nanosheets. Gratifyingly, the construction of heterojunction obviously elevates the PCR activities. In particular, the total CO₂ photoreduction conversion rates have increased by 2.75 and 4.43 times compared with the pristine ZnIn₂S₄ and TiO₂, respectively, attaining 18.32 μmol h⁻¹ g⁻¹. Moreover, this PCR reaction performance is higher than that of many other photocatalysts under similar conditions (Table S2, Supporting Information). Interestingly, undetected hydrogen is owing to the fact that the gas (CO₂+H₂O)-solid (photocatalyst) reaction system is more favorable for adsorption and activation of CO₂, thus the hydrogen evolution reaction is inhibited.^[66,67] Besides, the amount of photooxidation product O₂ was also close to its theoretical value (Table S3, Supporting Information). Meanwhile, the oxygen evolution rate of TiO₂@ZnIn₂S₄ is obviously higher than those of pristine ZnIn₂S₄ nanosheets and TiO₂ hollow spheres (Figure 5a). Based on the above analysis, the improvement of PCR performance can be ascribed to construction of S-scheme heterojunction. The TiO₂@ZnIn₂S₄ S-scheme heterojunction can efficiently facilitate the separation and transfer of photogenerated carriers. Meanwhile, a large number of useful photogenerated electrons with strong reduction ability can be retained in the CB of ZnIn₂S₄ to the CO₂ photoreduction reaction, while the photogenerated holes with strong oxidation ability can be retained in the VB of TiO₂ to the H₂O photooxidation reaction. Besides, the PCR performance of TiO₂@ZnIn₂S₄ nearly retains after running for three cycles (Figure 5b). XRD of TiO₂@ZnIn₂S₄ shows no noticeable change before and after PCR reaction (Figure 5c), suggesting the good stability of the TiO₂@ZnIn₂S₄ heterojunction. Moreover, to investigate the carbon origin of photoreduction products, ¹³CH₄ (*m/z* = 17) and ¹³CO (*m/z* = 29) characteristic peaks are detected in ¹³C-labeled CO₂, and ¹²CH₄ (*m/z* = 16) and ¹²CO (*m/z* = 28) are detected in ¹²C-labeled CO₂

sources by gas chromatography-mass spectrometry under the same conditions (Figure S6, Supporting Information). These results indicate that the detected photoreduction products originate from CO₂ instead of impurities.

Additionally, it is widely known that larger specific surface area of photocatalysts is beneficial to PCR reaction owing to the fact that it can provide the abundant active sites.^[19,37] Therefore, the surface area was evaluated via nitrogen adsorption-desorption isotherms. As shown in Figure 6a, all the samples display typical type IV isotherms with the type H3 hysteresis loop, signifying their mesoporous structures.^[45,47,54] Meanwhile, the pore-size distribution curves further testify their mesoporous structures (Figure 6a (inset)). Moreover, Brunauer–Emmett–Teller surface area (*S*_{BET}) of TiO₂@ZnIn₂S₄ (107 m² g⁻¹) is larger than those of TiO₂ (78 m² g⁻¹) and ZnIn₂S₄ (102 m² g⁻¹) (Table S4, Supporting Information). Besides, large specific surface area of the composite can supply abundant surface active and adsorption sites, which is favorable for the capture and activation of CO₂. Meanwhile, as shown in Figure 6b, the CO₂ adsorption capacity of TiO₂@ZnIn₂S₄ (0.12 mmol g⁻¹) is higher than those of TiO₂ (0.09 mmol g⁻¹) and ZnIn₂S₄ (0.10 mmol g⁻¹). Besides, the adsorption energy (*E*_{ad}) of CO₂ on ZnIn₂S₄ (-0.09 eV) is more negative than that on TiO₂ (-0.06 eV) (Figure S7, Supporting Information), which indicates that the adsorbed CO₂ on ZnIn₂S₄ is more stable than that on TiO₂. Together, all of these results confirm the superiority of TiO₂@ZnIn₂S₄ over pristine TiO₂ and ZnIn₂S₄ in PCR.

To further clarify the excellent CO₂ photoreduction activity of TiO₂@ZnIn₂S₄, photoluminescence (PL) and photoelectrochemical characterizations were performed. As displayed in Figure 6c, the steady-state PL intensity of TiO₂@ZnIn₂S₄ is obviously lower than those of pristine TiO₂ and ZnIn₂S₄, indicating that construction of S-scheme heterojunction photocatalyst can largely inhibit the recombination of photogenerated charge carriers.^[55,58] Moreover, as shown in Figure 6d, the average PL lifetime (*τ*_{ave}) of TiO₂@ZnIn₂S₄ (2.43 ns) is obviously shorter than those of pristine TiO₂ (3.35 ns) and ZnIn₂S₄ (4.81 ns), confirming a more efficient separation and transfer of photogenerated carriers in the S-scheme heterojunction.^[23,45,47,55,58] Additionally, TiO₂@ZnIn₂S₄ heterojunction shows the smaller electrochemical impedance spectroscopy (EIS) radius and higher photocurrent density than those of

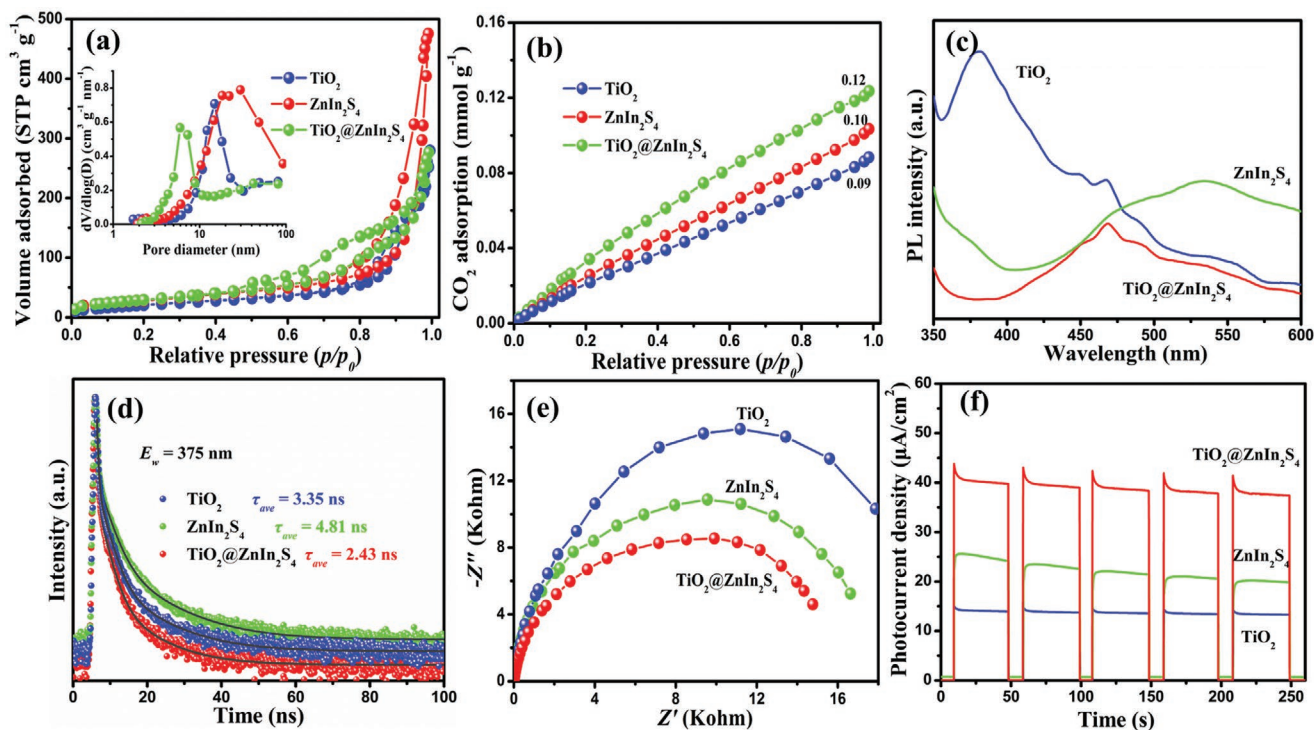


Figure 6. a) Nitrogen adsorption-desorption isotherms and pore-size distribution curves (inset), b) CO₂ adsorption isotherms, c) steady-state photoluminescence (PL) spectra, d) time-resolved PL spectra, e) electrochemical impedance spectroscopy (EIS) spectra, and f) transient photocurrent spectra of TiO₂, ZnIn₂S₄ and TiO₂@ZnIn₂S₄.

pristine TiO₂ and ZnIn₂S₄ (Figure 6e,f), reaffirming the highly efficient photogenerated charge carriers separation and transfer over TiO₂@ZnIn₂S₄ heterojunction.^[45,47,58,62,64] For comparison, control experiments indicate that the PCR performance of a physical mixture of TiO₂ and ZnIn₂S₄ (TiO₂-ZnIn₂S₄) is much inferior to that of TiO₂@ZnIn₂S₄ under the same condition (Figure S8a, Supporting Information). Besides, the EIS radius of TiO₂-ZnIn₂S₄ is much larger than that of TiO₂@ZnIn₂S₄ (Figure S8b, Supporting Information). Therefore, these results imply that the crucial roles of intimate interfacial contact and hierarchical core-shell hollow structures in TiO₂@ZnIn₂S₄ heterojunction for PCR reaction.

In situ diffuse reflectance infrared Fourier transform spectroscopy (in situ DRIFTS) can be used to directly detect the carbon-based groups formed on the surface of photocatalyst during the PCR reaction, which is helpful to analyze the formation mechanism of reaction intermediates.^[68] Therefore, to get further insight into the evolution process of PCR over the surface of TiO₂@ZnIn₂S₄, in situ DRIFTS was analyzed. As shown in Figure 7a, without introducing CO₂ and H₂O gas in the dark, no absorption peaks can be detected (Figure 7a(i)). When introducing CO₂ and H₂O gas without light irradiation (Figure 7a(ii)), bicarbonate species (HCO₃⁻, 1223, 1239, 1395 and 1449 cm⁻¹), monodentate carbonate species (m-CO₃²⁻, 1303, 1422, 1488, 1541

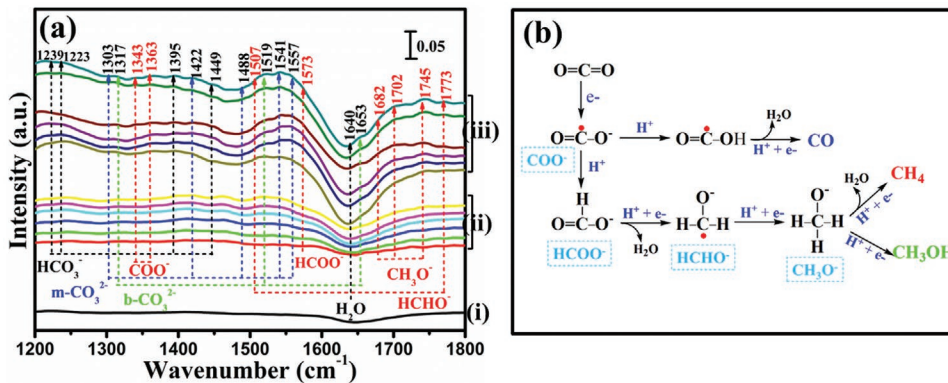


Figure 7. a) In situ diffuse reflectance infrared Fourier transform spectroscopy (DRIFTS) spectra of TiO₂@ZnIn₂S₄. b) Possible photocatalytic CO₂ reduction (PCR) reaction pathways on the surface of TiO₂@ZnIn₂S₄. The blue dashes boxes highlight the key intermediate species during photocatalytic CO₂ reduction (PCR) reaction.

and 1557 cm^{-1}) and bidentate carbonate species (b-CO_3^{2-} , 1317, 1519 and 1653 cm^{-1}) can be detected.^[39,55,58] These peaks mean that the CO_2 and H_2O are effectively adsorbed and activated on the surface of $\text{TiO}_2@Zn\text{In}_2\text{S}_4$. Furthermore, some new peaks can be observed under irradiation condition (Figure 7a(iii)). The emerging peaks can be attributed to carboxylate species (COO^- , 1342 and 1363 cm^{-1}), formaldehyde species (HCHO^- , 1507 and 1773 cm^{-1}), formic acid species (HCOO^- , 1573 cm^{-1}) and methoxy groups (CH_3O^- , 1682, 1702 and 1745 cm^{-1}).^[39,55,58] Meanwhile, these peaks of intermediates reveal that the effective photocatalytic activation and reaction of CO_2 occur on the surface of $\text{TiO}_2@Zn\text{In}_2\text{S}_4$. Based on the previous reports,^[2,3,39,55,58] the COO^- , HCHO^- , HCOO^- and CH_3O^- species are assigned to the important intermediates of PCR reaction. Therefore, according to analysis on the above of intermediate species, a possible CO_2 photoreduction conversion pathway over $\text{TiO}_2@Zn\text{In}_2\text{S}_4$ surface can be proposed in Figure 7b. Under light irradiation, CO_2 molecules are adsorbed and activated on $\text{TiO}_2@Zn\text{In}_2\text{S}_4$ surface. First, the photogenerated electrons react with the activated CO_2 molecules to form COO^- intermediate species. Partial COO^- recombine with protons to form $\cdot\text{COOH}$ radicals. Afterwards, $\cdot\text{COOH}$ radicals react with protons and photogenerated electrons to form H_2O and CO . The rest of COO^- intermediate radicals undergo further reaction with protons to form HCOO^- intermediate species. Subsequently, HCOO^- further accepts protons and photogenerated electrons to form HCHO^- species. Subsequently, HCHO^- species can be further converted into CH_3O^- intermediate species by reacting with the protons and photogenerated electrons. Finally, CH_3OH and CH_4 are generated. Therefore, the PCR conversion pathway over the surface of S-scheme $\text{TiO}_2@Zn\text{In}_2\text{S}_4$ CSHS follows the formaldehyde pathway.^[2,3,58,69]

3. Conclusions

In summary, hierarchical S-scheme $\text{TiO}_2@Zn\text{In}_2\text{S}_4$ CSHS heterojunction is successfully fabricated by growing ZnIn_2S_4 nanosheets on the outer surface of TiO_2 hollow spheres for efficient PCR reaction. The S-scheme charge transfer mechanism is revealed by in situ irradiated XPS, work function calculation and EPR measurements. The PCR performance of S-scheme $\text{TiO}_2@Zn\text{In}_2\text{S}_4$ heterojunction photocatalyst is significantly improved. The total CO_2 photoreduction conversion rates (the sum yield of CO , CH_3OH and CH_4) of S-scheme $\text{TiO}_2@Zn\text{In}_2\text{S}_4$ heterojunction have increased by 2.75 and 4.43 times compared with the pristine ZnIn_2S_4 and TiO_2 , respectively. Experimental results demonstrate that this rational design can not only effectively facilitate the separation of useful photogenerated electrons and holes, but also provide large surface areas and abundant active sites for multi-electron PCR reaction. Therefore, this work provides a feasible approach to address the formation and photogenerated charge transfer mechanism of heterojunction photocatalysts without cocatalysts and sacrificial agents for the gas-solid PCR reaction system.

Supporting Information

Supporting Information is available from the Wiley Online Library or from the author.

Acknowledgements

This work was supported by the National Natural Science Foundation of China (NSFC) (Nos. 51932007, 51872220, 51961135303, 21871217, 52073223, U1905215, and U1705251), the Fundamental Research Funds for the Central Universities (No. WUT: 2021IVA137), and the Innovative Research Funds of Foshan Xianhu Laboratory of the Advanced Energy Science and Technology Guangdong Laboratory (XHD2020-001).

Conflict of Interest

The authors declare no conflict of interest.

Data Availability Statement

Research data are not shared.

Keywords

charge transfer, core-shell, hollow structures, S-scheme mechanism, step-scheme heterojunction

Received: June 13, 2021

Revised: July 18, 2021

Published online:

- [1] C. Bie, H. Yu, B. Cheng, W. Ho, J. Fan, J. Yu, *Adv. Mater.* **2021**, *33*, 2003521.
- [2] T. Kong, Y. Jiang, Y. Xiong, *Chem. Soc. Rev.* **2020**, *49*, 6579.
- [3] Z. Sun, N. Talreja, H. Tao, J. Texter, M. Muhler, J. Strunk, J. Chen, *Angew. Chem., Int. Ed.* **2018**, *57*, 7610.
- [4] S. Das, J. Pérez-Ramírez, J. Gong, N. Dewangan, K. Hidajat, B. Gates, S. Kawi, *Chem. Soc. Rev.* **2020**, *49*, 2937.
- [5] Y. Xia, Z. Tian, T. Heil, A. Meng, B. Cheng, S. Cao, J. Yu, M. Antonietti, *Joule* **2019**, *3*, 2792.
- [6] Z. Pan, M. Liu, P. Niu, F. Guo, X. Fu, X. Wang, *Acta Phys.-Chim. Sin.* **2020**, *36*, 1906014.
- [7] U. Ulmer, T. Dingle, P. Duchesne, R. Morris, A. Tavasoli, T. Wood, G. Ozin, *Nat. Commun.* **2019**, *10*, 3169.
- [8] H. Wang, Y. Wang, L. Guo, X. Zhang, C. Ribeiro, T. He, *Chin. J. Catal.* **2020**, *41*, 131.
- [9] Y. Zhou, Z. Wang, L. Huang, S. Zaman, K. Lei, T. Yue, Z. Li, B. You, B. Xia, *Adv. Energy Mater.* **2021**, *11*, 2003159.
- [10] A. Crake, K. Christoforidis, A. Gregg, B. Moss, A. Kafizas, C. Petit, *Small* **2019**, *15*, 1805473.
- [11] J. He, C. Janáky, *ACS Energy Lett.* **2020**, *5*, 1996.
- [12] V. Rodríguez-González, S. Obregón, O. Patrón-Soberano, C. Terashima, A. Fujishima, *Appl. Catal., B* **2020**, *270*, 118853.
- [13] R. Wang, M. Shi, F. Xu, Y. Qiu, P. Zhang, K. Shen, Q. Zhao, J. Yu, Y. Zhang, *Nat. Commun.* **2020**, *11*, 4465.
- [14] A. Meng, B. Cheng, H. Tan, J. Fan, C. Su, J. Yu, *Appl. Catal., B* **2021**, *289*, 120039.
- [15] J. Li, X. Wu, S. Liu, *Acta Phys.-Chim. Sin.* **2021**, *37*, 2009038.
- [16] X. Zhou, *Acta Phys.-Chim. Sin.* **2021**, *37*, 2008064.
- [17] A. Mamaghani, F. Haghghat, C. Lee, *Appl. Catal., B* **2020**, *269*, 118735.
- [18] H. Tang, Y. Ren, S. Wei, G. Liu, X. Xu, *Rare Met.* **2019**, *38*, 453.
- [19] C. Xu, P. Anusuyadevi, C. Aymonier, R. Luque, S. Marre, *Chem. Soc. Rev.* **2019**, *48*, 3868.
- [20] L. Wang, B. Zhu, B. Cheng, J. Zhang, L. Zhang, J. Yu, *Chin. J. Catal.* **2021**, *42*, 1648.

- [21] J. Tan, S. Gavrielides, M. Belekoukia, W. Thompson, L. Negahdar, F. Xia, M. Maroto-Valer, A. Beale, *Chem. Commun.* **2020**, 56, 12150.
- [22] J. Wang, G. Wang, B. Cheng, J. Yu, J. Fan, *Chin. J. Catal.* **2021**, 42, 56.
- [23] F. Xu, K. Meng, B. Cheng, S. Wang, J. Xu, J. Yu, *Nat. Commun.* **2020**, 11, 4613.
- [24] Z. Wang, Y. Chen, L. Zhang, B. Cheng, J. Yu, J. Fan, *J. Mater. Sci. Technol.* **2020**, 56, 143.
- [25] X. Lian, W. Xue, S. Dong, E. Liu, H. Li, K. Xu, *J. Hazard. Mater.* **2021**, 412, 125217.
- [26] S. Wageh, A. Al-Ghamdi, R. Jafer, X. Li, P. Zhang, *Chin. J. Catal.* **2021**, 42, 667.
- [27] Q. Xu, L. Zhang, B. Cheng, J. Fan, J. Yu, *Chem* **2020**, 6, 1543.
- [28] Z. Li, Z. Wu, R. He, L. Wan, S. Zhang, *J. Mater. Sci. Technol.* **2020**, 56, 151.
- [29] X. Fei, H. Tan, B. Cheng, B. Zhu, L. Zhang, *Acta Phys.-Chim. Sin.* **2021**, 37, 2010027.
- [30] R. He, H. Liu, H. Liu, D. Xu, L. Zhang, *J. Mater. Sci. Technol.* **2020**, 52, 145.
- [31] C. Cheng, B. He, J. Fan, B. Cheng, S. Cao, J. Yu, *Adv. Mater.* **2021**, 33, 2100317.
- [32] P. Xia, S. Cao, B. Zhu, M. Liu, M. Shi, J. Yu, Y. Zhang, *Angew. Chem., Int. Ed.* **2020**, 59, 5218.
- [33] S. Wageh, A. Al-Ghamdi, L. Liu, *Acta Phys.-Chim. Sin.* **2021**, 37, 2010024.
- [34] L. Liu, T. Hu, K. Dai, J. Zhang, C. Liang, *Chin. J. Catal.* **2021**, 42, 46.
- [35] Y. Ren, Y. Li, X. Wu, J. Wang, G. Zhang, *Chin. J. Catal.* **2020**, 42, 69.
- [36] W. Wang, W. Zhao, H. Zhang, X. Dou, H. Shi, *Chin. J. Catal.* **2021**, 42, 97.
- [37] Y. Wei, N. Yang, K. Huang, J. Wan, F. You, R. Yu, S. Feng, D. Wang, *Adv. Mater.* **2020**, 32, 2002556.
- [38] C. Nguyen, N. Vu, T. Do, *J. Mater. Chem. A* **2015**, 3, 18345.
- [39] C. Bie, B. Zhu, F. Xu, L. Zhang, J. Yu, *Adv. Mater.* **2019**, 31, 1902868.
- [40] Z. Hu, X. Li, S. Zhang, Q. Li, J. Fan, X. Qu, K. Lv, *Small* **2020**, 16, 2004583.
- [41] M. Xiao, Z. Wang, M. Lyu, B. Luo, S. Wang, G. Liu, H. M. Cheng, L. Wang, *Adv. Mater.* **2019**, 31, 1801369.
- [42] S. Wang, Y. Wang, S. Zang, X. Lou, *Small Methods* **2020**, 4, 1900586.
- [43] Y. Wang, S. Wang, L. Zhang, X. Lou, *Angew. Chem., Int. Ed.* **2020**, 59, 11918.
- [44] P. Zhang, X. Lou, *Adv. Mater.* **2019**, 31, 1900281.
- [45] S. Wang, B. Guan, X. Lou, *J. Am. Chem. Soc.* **2018**, 140, 5037.
- [46] Y. Xia, B. Cheng, J. Fan, J. Yu, G. Liu, *Sci. China Mater.* **2020**, 63, 552.
- [47] S. Wang, Y. Wang, S. Zhang, S. Zang, X. Lou, *Adv. Mater.* **2019**, 31, 1903404.
- [48] D. Majhi, K. Das, R. Bariki, S. Padhan, A. Mishra, R. Dhiman, P. Dash, B. Nayak, B. Mishra, *J. Mater. Chem. A* **2020**, 8, 21729.
- [49] A. Chachvalvutikul, T. Luangwanta, S. Pattisson, G. Hutchings, S. Kaowphong, *Appl. Surf. Sci.* **2020**, 544, 148885.
- [50] Q. Han, L. Li, W. Gao, Y. Shen, L. Wang, Y. Zhang, X. Wang, Q. Shen, Y. Xiong, Y. Zhou, *ACS Appl. Mater. Interfaces* **2021**, 13, 15092.
- [51] G. Zhang, D. Chen, N. Li, Q. Xu, H. Li, J. He, J. Lu, *Angew. Chem., Int. Ed.* **2020**, 132, 8332.
- [52] Z. Mei, G. Wang, S. Yan, J. Wang, *Acta Phys.-Chim. Sin.* **2021**, 37, 2009097.
- [53] W. Stöber, A. Fink, E. Bohn, *J. Colloid Interface Sci.* **1968**, 26, 62.
- [54] H. Liu, W. Li, D. Shen, D. Zhao, G. Wang, *J. Am. Chem. Soc.* **2015**, 137, 13161.
- [55] F. He, B. Zhu, B. Cheng, J. Yu, W. Ho, W. Macyk, *Appl. Catal., B* **2020**, 272, 119006.
- [56] P. Zhang, Y. Li, Y. Zhang, R. Hou, X. Zhang, C. Xue, S. Wang, B. Zhu, N. Li, G. Shao, *Small Methods* **2020**, 4, 2000214.
- [57] J. Low, B. Dai, T. Tong, C. Jiang, J. Yu, *Adv. Mater.* **2019**, 31, 1802981.
- [58] L. Wang, H. Tan, L. Zhang, B. Cheng, J. Yu, *Chem. Eng. J.* **2021**, 411, 128501.
- [59] Z. Xing, J. Hu, M. Ma, H. Lin, Y. An, Z. Liu, Y. Zhang, J. Li, S. Yang, *J. Am. Chem. Soc.* **2019**, 141, 19715.
- [60] Y. Xia, B. Cheng, J. Fan, J. Yu, G. Liu, *Small* **2019**, 15, 1902459.
- [61] H. Deng, X. Fei, Y. Yang, J. Fan, J. Yu, B. Cheng, L. Zhang, *Chem. Eng. J.* **2020**, 409, 127377.
- [62] T. He, L. Wang, F. Fabregat-Santiago, G. Liu, Y. Li, C. Wang, R. Guan, *J. Mater. Chem. A* **2017**, 5, 6455.
- [63] Y. Chiu, K. Chang, Y. Hsu, *J. Mater. Chem. A* **2018**, 6, 4286.
- [64] Z. He, Y. Han, S. Liu, W. Cui, Y. Qiao, T. He, Q. Wang, *ChemElectroChem* **2020**, 7, 4390.
- [65] Z. Yang, Y. Qi, F. Wang, Z. Han, Y. Jiang, H. Han, J. Liu, X. Zhang, W. Ong, *J. Mater. Chem. A* **2020**, 8, 24868.
- [66] L. Pei, Y. Yuan, W. Bai, T. Li, H. Zhu, Z. Ma, J. Zhong, S. Yan, Z. Zou, *ACS Catal.* **2020**, 10, 15083.
- [67] F. Chen, H. Huang, L. Ye, T. Zhang, Y. Zhang, X. Han, T. Ma, *Adv. Funct. Mater.* **2018**, 28, 1804284.
- [68] X. Li, S. Wang, L. Li, Y. Sun, Y. Xie, *J. Am. Chem. Soc.* **2020**, 142, 9567.
- [69] S. Habisreutinger, L. Schmidt-Mende, J. Stolarczyk, *Angew. Chem., Int. Ed.* **2013**, 52, 7372.